THE ASTRONOMICAL JOURNAL, 119:3003–3014, 2000 June
© 2000. The American Astronomical Society. All rights reserved. Printed in U.S.A.

A SEARCH FOR OH MEGAMASERS AT $z > 0.1$. I. PRELIMINARY RESULTS

JEREMY DARLING AND RICCARDO GIOVANELLI
Department of Astronomy, Cornell University, Ithaca, NY 14853; darling@astrosun.tn.cornell.edu; riccardo@astrosun.tn.cornell.edu
Received 1999 December 8; accepted 2000 March 7

ABSTRACT

We present the preliminary results of a survey for OH megamasers underway at the Arecibo Observatory.[1] The goals of the survey are to calibrate the luminosity function of OH megamasers to the low-redshift galaxy merger rate ($0.1 < z < 0.2$) and to use the enhanced sample of OH megamasers provided by the survey to study OH megamaser environments, engines, lifetimes, and structure. The survey should double the known OH megamaser sample to roughly 100 objects. Survey results will be presented in installments to facilitate community access to the data. Here we report the discovery of 11 OH megamasers and one OH absorber, and we include upper limits on the isotropic 1667 MHz OH line luminosity of 53 other luminous infrared galaxies at $z > 0.1$. The new megamasers show a wide range of spectral properties but are consistent with the extant set of 55 previously reported objects, only eight of which have $z > 0.1$.

Key words: galaxies: evolution — galaxies: interactions — galaxies: nuclei — infrared radiation — masers — radio emission lines

1. INTRODUCTION

All known OH megamasers (OHMs) have been observed in luminous infrared galaxies, strongly favoring the most FIR-luminous, the ultraluminous infrared galaxies (ULIRGs; Baan 1991). Photometric surveys have shown the ULIRGs to be nearly exclusively the product of galaxy mergers (Clements et al. 1996). VLBI measurements have shown that OHMs are ensembles of many masing regions, which originate in the nuclear regions of (U)LIRGs within scales of a few hundred parsecs or less (Diamond et al. 1999). OHM activity requires: (1) high molecular density, (2) a pump to invert the hyperfine population of the OH ground state, and (3) a source of 18 cm continuum emission to stimulate maser emission (Burdyuzha & Komberg 1990). The galaxy merger environment can supply all of these requirements: the merger interaction concentrates molecular gas in the merger nuclei, creates strong FIR dust emission from reprocessed starburst light and AGN activity, and produces radio continuum emission from AGN or starbursts. Either the FIR radiation field or collisional shocks in the molecular gas can invert the OH population via the pumping lines at 35 and 53 μm. Masing can then be stimulated by 18 cm continuum emission from starbursts or AGN, or even by spontaneous emission from the masing cloud itself (Henkel, Güsten, & Baan 1987).

The FIR luminosity of ULIRGs seems to be correlated with the merger sequence phase, based on optical morphology and surface brightness profiles (Sanders, Surace, & Ishida 1999). OHM fraction in ULIRGs is a strong function of $L_{\rm FIR}$ (see Baan 1991 and Fig. 3), which would indicate a preferred time during the merger sequence for OHM formation. This makes some physical sense, based on the high molecular gas density required to produce OHMs ($n_{\rm H_2} = 10^{4-7}$ cm^{-3}; Baan 1991). Early in the merger sequence infall and concentration of molecular gas in the nuclear regions is just beginning, whereas late in the merger sequence clouds are disrupted by ionizing radiation, a superwind phase, or a QSO eruption. If OHMs mark a specific phase in major mergers, then they provide useful tracers of the galaxy merger rate as a function of redshift, particularly since they may be observed at cosmological distances with current instrumentation (Baan 1989; Burdyuzha & Komberg 1990; Briggs 1998).

Many studies of the high-redshift galaxy luminosity function indicate that the galaxy population has undergone either luminosity evolution, number density evolution, or both since $z \sim 0.7$ (Lilly et al. 1995; Ellis et al. 1996). The only way to disentangle the two effects in galaxy evolution is to directly study the evolution of the galaxy number density, which depends on the galaxy merger rate. Morphological evolution of field galaxies hints that mergers may be important: *HST* surveys indicate a morphological evolution of field galaxies, with a larger proportion of faint irregular galaxies in the past compared to the present (Brinchmann et al. 1998). The connection between gross morphological evolution and mergers seems to be supported by surveys aimed at the detection of the morphological signatures of merger activity. Several morphological merger surveys have measured an increase in merger fraction with redshift (Le Févre et al. 2000; Patton et al. 1997). Evolution of the number density of galaxies is a key component of hierarchical models of galaxy formation, and measurements of the merger rate as a function of redshift should provide meaningful constraints on galaxy formation models (see Abraham 1999 for a review).

The merger rate, or merger fraction, of galaxies can be measured by surveys targeting the observable signatures of merger activity, which include: (1) strong FIR dust emission, (2) enhanced star formation and/or AGN activity, (3) morphological irregularities, such as tidal tails, rings, filaments, or shells, and (4) enhanced molecular gas emission, including OH masing.

Detection of enhanced FIR dust emission from ULIRGs is currently limited to $z \lesssim 0.3$ by the sensitivity of the *Infrared Astronomical Satellite* (*IRAS*) at 60 μm (Clements, Saunders, & McMahon 1999). Hence the merger rate of galaxies

[1] The Arecibo Observatory is part of the National Astronomy and Ionosphere Center, which is operated by Cornell University under a cooperative agreement with the National Science Foundation.

can be measured using ULIRG surveys, but only at very low redshifts. High-redshift counterparts to ULIRGs appear to be the submillimeter galaxies detected at redshifts of roughly 1–3 (Cowie & Barger 2000; Smail et al. 2000). Only a few of the submillimeter galaxies have measured redshifts, a task made difficult by high optical/UV extinction in these sources. A meaningful measure of the merger rate based on submillimeter detections may be premature at this time.

The most promising method for measuring the galaxy merger rate up to $z = 1$ relies on the morphological disturbances present in mergers. Several groups have used morphological and close pair surveys to measure the merger fraction (see Le Févre et al. 2000; Patton et al. 1997), and Le Févre et al. have determined a power-law dependence of merger fraction on redshift with slope $(1 + z)^{3.4}$ up to $z = 0.91$. The approach requires high angular resolution and high sensitivity to identify the faint debris associated with mergers. Flux-limited morphology surveys suffer from the bias produced by the brightening associated with galaxy interactions and the extinction produced in advanced mergers as molecular gas and dust is concentrated into the central regions of merging galaxies. Morphological surveys are also likely to omit advanced mergers that have a single envelope and two closely separated nuclei.

Finally, one might measure the merger rate of galaxies using OHMs as tracers of merger activity (Burdyuzha & Komberg 1990; Briggs 1998). This is an avenue as yet unexplored, and the role of OHMs in mergers remains poorly understood. If one can calibrate the OHM fraction in ULIRGs as a function of $L_{\rm FIR}$ at low redshifts (which can be related to the low-redshift merger fraction), then surveys for OHMs at higher redshifts can yield a measure of the merger rate of galaxies as a function of cosmic time. This technique relies on the assumption that OHMs are a constant fraction of ULIRGs as a function of cosmic time, which seems to be a reasonable assumption given the weak dependence of metallicity on redshift in the nuclear regions of massive spiral galaxies. Using OHMs to trace merger activity has several advantages over other techniques: (1) OHM emission lines are detectable at much greater distances than FIR emission with current instrumentation, (2) detection of OHMs does not rely on high angular resolution and does not exclude advanced mergers, and (3) OHM detection favors the large column densities produced in merger environments, which tend to cause extinction in the optical and NIR regime.

The primary goal of this OHM survey is to determine the incidence of OHMs in ULIRGs as a function of FIR luminosity, in order to relate the luminosity function of OHMs to the low redshift galaxy merger rate ($0.1 < z < 0.2$). This will allow subsequent workers to estimate the galaxy merger rate at higher redshifts from blind or targeted OHM surveys. Note that previous OHM surveys have obtained estimates of the OHM fraction in LIRGs, but all are subject to large uncertainties due to small numbers of detections (Norris et al. 1989; Staveley-Smith et al. 1992; Baan, Haschick, & Henkel 1992; and others). One might expect the galaxy merger rate to roughly follow the evolution of quasars (see Kim & Sanders 1998 and Le Févre et al. 2000), but this notion has not yet been confirmed. A useful side benefit of the survey will be a doubling of the OHM sample and a sixfold increase in the $z > 0.1$ OHM sample. We intend to use the enhanced sample to study OHM environments, lifetimes, engines, and structure. This paper presents the results of the preliminary phase of the survey, which targets a FIR selected, flux-limited sample of about 300 sources, 69 of which have been observed to date. Results will be presented in installments to facilitate community access to the data.

In this paper, we describe the methods used for a new search for OHMs (§ 2); we present and discuss the OH detections as well as the nondetections, including upper limits on OH luminosity in nondetections (§ 3); we evaluate the detection rate of our candidate selection methods, and discuss the new sample of OHMs (§ 4); and we predict the final outcome of the survey, and discuss future prospects (§ 5).

This paper parameterizes the Hubble constant as $H_0 = 75\ h_{75}$ km s^{-1} Mpc^{-1}, assumes $q_0 = 0$, and uses $D_L = (v_{\rm CMB}/H_0)\ (1 + 0.5 z_{\rm CMB})$ to compute luminosity distances from $v_{\rm CMB}$, the cosmic microwave background (CMB) rest-frame velocity.

2. SEARCH CRITERIA AND OBSERVATIONS

Prior to this work, 55 OHMs were reported, which exhibit a wide range of characteristics (see Baan, Salzer, & LeWinter 1998 for a listing of 52 OHMs). This sample revealed a relationship between the FIR luminosity and the isotropic OH luminosity of OHMs, which was originally thought to be quadratic ($L_{\rm OH} \propto L^2_{\rm FIR}$; see Baan 1989). As discussed by Kandalian (1996), Malmquist bias affects both OH detection and FIR selection of OHM candidates from the *IRAS* data, and the two data sets are biased differently. Hence, the correlation of $L_{\rm FIR}$ and $L_{\rm OH}$ with fixed D_L would necessarily create a correlation between the two variables. This third variable correlation must be removed to determine the true correlation between $L_{\rm FIR}$ and $L_{\rm OH}$ for fixed $\rm I_L$. Kandalian uses the partial correlation coefficient method for 49 OHMs, which reveals a $L_{\rm OH}$-$L_{\rm FIR}$ relationship more linear than quadratic: $\log L_{\rm OH} = (1.38 \pm 0.14) \log L_{\rm FIR} - (14.02 \pm 1.66)$. Diamond et al. (1999) suggest that this relationship represents an admixture of unsaturated maser emission (quadratic relationship) and saturated maser emission (linear relationship) from diffuse and compact OH masing regions, respectively. In either case, a useful selection criterion for locating new OHMs is the requirement for strong FIR emission from a candidate host, typically $\log (L_{\rm FIR}/L_\odot) \geq 11.0$.

OHM candidates were selected from the Point Source Catalog redshift survey (PSCz; W. Saunders 1999, private communication), supplemented by the NASA/IPAC Extragalactic Database.[2] The PSCz catalog is a flux-limited (*IRAS* $f_{60\ \mu{\rm m}} > 0.6$ Jy) redshift survey of 15,000 *IRAS* galaxies over 84% of the sky (see Saunders et al. 2000). We select *IRAS* sources that are in the Arecibo sky ($0° < \delta < 37°$), that were detected at 60 μm, and that have $0.1 \leq z \leq 0.45$. The lower redshift bound is set to avoid local radio frequency interference (RFI), while the upper bound is set by the bandpass of the wide L-band receiver at Arecibo. No constraints are placed on FIR colors or luminosity. The redshift requirement limits the number of candidates in the Arecibo sky to 377. Of these 296 are found in

[2] The NASA/IPAC Extragalactic Database (NED) is operated by the Jet Propulsion Laboratory, California Institute of Technology, under contract with the National Aeronautics and Space Administration.

the PSCz survey. The condition that candidates have $z > 0.1$ automatically selects (U)LIRGs, if they were detected by *IRAS* at 60 μm. The strong influence of $L_{\rm FIR}$ on the OHM fraction in ULIRGs is the primary reason for our high detection rate compared with previous surveys (see, e.g., Staveley-Smith et al. 1992 and Baan et al. 1992).

The upgraded Arecibo radio telescope offers new opportunities for the detection of OHMs, because of its improved sensitivity, frequency agility, and instantaneous spectral coverage. Its large collecting area makes it ideal for a survey of spectral lines at the upper end of the redshift range of the known OHM sample ($0.1 \leq z \leq 0.3$). Detection of OH emission lines is generally possible in a 4 minute integration, even for $z \simeq 0.2$. In roughly 200 hr, we expect to observe about 300 OHM candidates and double the sample of OHMs (see § 5).

Observations were performed at Arecibo by nodding on- and off-source in 4 minute intervals, followed by firing a noise diode after each off-source integration. Spectra were recorded every 6 s to facilitate RFI removal. Data were recorded with nine-level sampling in two polarizations of 1024 channels each, spanning 25 MHz. The bandpass was centered on 1666.38 MHz (the mean of the 1667 and 1665 MHz lines), redshifted appropriately for each source. Strong, sharp RFI features were flagged in the 6 s records using a broad Hanning filter and a power threshold in the following manner: (1) each spectrum was Hanning smoothed with nine-point sampling and subtracted from the original unsmoothed spectrum, and (2) channels with $>1\%$ of the total power were flagged as RFI. Each 4 minute on-off pair was converted to system temperature units, then to flux density units (mJy) using a noise diode, which was calibrated to VLA flux standards. Baselines were fitted and subtracted from each on-off pair, and multiple pairs were combined via a noise-weighted average. Polarizations were averaged, and the final spectra were Hanning smoothed. The frequency resolution after Hanning smoothing is 49 kHz. The uncertainty in the absolute flux scale is 8%.

At the time of observations, the L-band wide receiver beam was slightly elliptical, with an average HPBW of 3.′4 at 1420.4 ± 6.25 MHz.[3] At 1500 MHz, the beam would have HPBW of 3.′2. The system temperature was 36 K at a zenith angle of 4° and increased monotonically to 40 K at ZA = 18°. The gain was roughly constant at 9.9 K Jy^{-1} up to ZA = 16° and decreased to 9.6 K Jy^{-1} at ZA = 18°.

3. RESULTS

Observations were made of 68 candidate OHMs, with $0° < \delta < 37°$, $0.10 \leq z \leq 0.45$, and $2^{\rm h} < \alpha < 23^{\rm h}$, from a set of 235 targets that satisfy these selection criteria. The completion is highest (68%) in $18^{\rm h} \leq \alpha \leq 22^{\rm h}$. Note that *IRAS* 19084+3719 falls outside of $0° < \delta < 37°$ but is included in the lists of nondetections.

Of the 68 candidates surveyed, 11 new OHMs and one new OH absorber were detected. Strong upper limits for OH luminosity can be placed on 53 nondetections. Three candidates were rejected because of RFI (*IRAS* F02054+0835, F13380+3339, and F15438+0438), and *IRAS* F15599+0206 was set aside because of strong radio continuum (see discussion of this selection effect below).

[3] See Arecibo Technical and Operations Memo 99-02 by C. Heiles at http://naic.edu/%7Edonna/performance.htm.

3.1. *Nondetections*

Tables 1 and 2 list, respectively, the optical/FIR and radio properties of the 54 OH nondetection ULIRGs. We can predict the expected $L_{\rm OH}$ for the OHM candidates, based on the $L_{\rm OH}$-$L_{\rm FIR}$ relation computed by Kandalian (1996; see § 2), and compare this figure with upper limits on $L_{\rm OH}$ derived from observations for a rough measure of the confidence of the nondetections. Table 1 lists the optical redshifts and FIR properties of the nondetections in the following format. Column (1): *IRAS* Faint Source Catalog (FSC) name. Columns (2) and (3): source coordinates (epoch B1950.0) from the FSC or the Point Source Catalog (PSC) if not available in the FSC. Columns (4), (5), and (6): heliocentric optical redshift, reference, and corresponding velocity. Uncertainties in velocities are listed whenever they are available. Column (7): cosmic microwave background rest-frame velocity. This is computed from the heliocentric velocity, using the solar motion with respect to the CMB measured by Lineweaver et al. (1996): $v_\odot = 368.7 \pm 2.5$ km s^{-1} toward $(l, b) = (264.^\circ31 \pm 0.^\circ16, 48.^\circ05 \pm 0.^\circ09)$. Column (8): luminosity distance computed from $v_{\rm CMB}$ via $D_L = (v_{\rm CMB}/H_0)\,(1 + 0.5 z_{\rm CMB})$, assuming $q_0 = 0$. Columns (9) and (10): *IRAS* 60 and 100 μm flux densities in Jy. FSC flux densities are listed whenever they are available. Otherwise, PSC flux densities are used. Uncertainties refer to the last digits of each measure, and upper limits on 100 μm flux densities are indicated by a less than symbol. Column (11): logarithm of the far-infrared luminosity in units of $L_\odot$. $L_{\rm FIR}$ is computed following the prescription of Fullmer & Lonsdale (1989): $L_{\rm FIR} = 3.96 \times 10^5 D_L^2 (2.58 f_{60} + f_{100})$, where f_{60} and f_{100} are the 60 and 100 μm flux densities expressed in Jy, D_L is in Mpc, and $L_{\rm FIR}$ is in units of $L_\odot$. If f_{100} is only available as an upper limit, the permitted range of $L_{\rm FIR}$ is listed. The lower bound on $L_{\rm FIR}$ is computed for $f_{100} = 0$ mJy, and the upper bound is computed with f_{100} set equal to its upper limit. The uncertainties in D_L and the flux densities typically produce an uncertainty in $\log L_{\rm FIR}$ of 0.01.

Table 2 lists the 1.4 GHz flux density and the limits on OH emission of the nondetections in the following format. Column (1): *IRAS* FSC name, as in Table 1. Column (2): heliocentric optical redshift, as in Table 1. Column (3): $L_{\rm FIR}$, as in Table 1. Column (4): predicted isotropic OH line luminosity, $\log L_{\rm OH}^{\rm pred}$, based on the Malmquist bias–corrected $L_{\rm OH}$-$L_{\rm FIR}$ relation determined by Kandalian (1996) for 49 OHMs: $\log L_{\rm OH} = (1.38 \pm 0.14) \log L_{\rm FIR} - (14.02 \pm 1.66)$ (see § 2). Column (5): upper limit on the isotropic OH line luminosity $\log L_{\rm OH}^{\rm max}$. The upper limits on $L_{\rm OH}$ are computed from the rms noise of the nondetection spectrum, assuming a boxcar line profile of rest-frame width $\Delta v = 150$ km s^{-1} and height 1.5 σ: $\log L_{\rm OH}^{\rm max} = \log \{4\pi D_L^2\ 1.5\ \sigma(\Delta v/c)[\nu_0/(1+z)]\}$. The assumed rest-frame width $\Delta v = 150$ km s^{-1} is the average FWHM of the 1667 MHz line of the known OHM sample. Column (6): on-source integration time, in minutes. Column (7): rms noise values in flat regions of the nondetection baselines in mJy, after spectra were Hanning smoothed to a spectral resolution of 49 kHz. Column (8): 1.4 GHz continuum fluxes, from the NRAO VLA Sky Survey (Condon et al. 1998). If no continuum source lies within 30″ of the *IRAS* coordinates, an upper limit of 5.0 mJy is listed. Column (9): optical spectroscopic classification, if available. Codes used are as follows: S2 = Seyfert type 2; S1.9 = Seyfert type 1.9; S1.5 = Seyfert type 1.5; S1 = Seyfert type 1; H = H II region (starburst); and L

TABLE 1

OH Nondetections: Optical Redshifts and FIR Properties

IRAS Name[a] (1)	α (2)	δ (3)	$z_{\odot}$ (4)	Ref. (5)	$v_{\odot}$ [b] (6)	$v_{\rm CMB}$ [b] (7)	D_L [c] (8)	f_{60} [d] (9)	f_{100} [d] (10)	$\log L_{\rm FIR}$ [e] (11)
02290+3139.....	02 29 05.6	+31 39 28	0.2115	2	63412 (105)	63188 (110)	931 (2)	0.567 (51)	1.39 (28)	11.99
03477+2611.....	03 47 43.3	+26 11 55	0.1494	2	44779 (196)	44645 (199)	640 (3)	0.711 (50)	1.36 (23)	11.71
03533+2606.....	03 53 19.9	+26 06 14	0.1883	7	56451 ( )	56324 (37)	822 (1)	0.414 (58)	<3.11	11.46–12.05
04046+1011.....	04 04 44.6	+10 11 55	0.1845	17	55312 (150)	55204 (154)	804 (2)	0.475 (38)	<4.38	11.50–12.16
08559+1053.....	08 55 58.8	+10 53 02	0.1480	1	44369 (70)	44661 (74)	640 (1)	1.119 (67)	1.95 (25)	11.89
13542+1040.....	13 54 18.1	+10 40 50	0.1234	3	37001 (46)	37263 (52)	528 (1)	0.797 (88)	0.60 (15)	11.47
14202+2615.....	14 20 16.0	+26 15 43	0.1590	1	47667 (70)	47868 (76)	689 (1)	1.492 (104)	1.99 (18)	12.04
14203+3005.....	14 20 19.4	+30 05 58	0.1141	10	34202 (26)	34393 (39)	485 (1)	0.960 (77)	1.39 (19)	11.56
15445+3312.....	15 44 32.1	+33 12 57	0.1558	11	46710 (81)	46796 (87)	673 (1)	0.383 (34)	0.86 (15)	11.52
15543+3013.....	15 54 22.7	+30 13 22	0.1213	11	36360 (81)	36439 (88)	515 (1)	0.393 (39)	0.68 (17)	11.25
15597+3133.....	15 59 47.3	+31 33 27	0.1437	11	43070 (81)	43140 (88)	617 (1)	0.466 (42)	1.11 (16)	11.54
16045+2733.....	16 04 33.8	+27 33 03	0.1139	10	34147 (22)	34217 (40)	482 (1)	0.828 (58)	1.77 (23)	11.56
16121+2611.....	16 12 08.7	+26 11 47	0.1310	12	39273 ( )	39335 (34)	559 (1)	0.191 (42)	<0.41	10.79–11.05
16156+0146.....	16 15 35.2	+01 46 42	0.1320	1	39573 (70)	39657 (79)	564 (1)	1.126 (68)	1.00 (22)	11.69
16284+2817.....	16 28 29.2	+28 17 17	0.0970	10	29080 (24)	29116 (42)	407 (1)	1.109 (55)	0.88 (25)	11.39
16474+3430.....	16 47 24.2	+34 30 18	0.1115	8	33418 (47)	33422 (58)	470 (1)	2.272 (114)	2.88 (20)	11.88
17030+0457.....	17 03 02.6	+04 57 45	0.1190	6	35675 (300)	35681 (302)	504 (5)	0.603 (42)	<1.84	11.19–11.53
17156+1238.....	17 15 36.9	+12 38 18	0.1130	7	33876 ( )	33857 (36)	477 (1)	0.778 (54)	<1.26	11.26–11.47
17490+2659.....	17 49 05.8	+26 59 46	0.1453	15	43560 ( )	43484 (34)	622 (1)	0.466 (42)	<1.37	11.27–11.60
17574+0629.....	17 57 26.4	+06 29 17	0.1096	8	32860 (44)	32779 (57)	461 (1)	2.075 (145)	<5.48	11.65–11.96
18030+0705.....	18 03 01.6	+07 05 39	0.1458	8	43708 (56)	43618 (67)	624 (1)	0.838 (75)	4.40 (48)	12.00
18040+2141.....	18 04 06.2	+21 41 06	0.1016	13	30454 (24)	30357 (42)	425 (1)	1.474 (133)	2.35 (35)	11.64
18147+1553.....	18 14 45.2	+15 53 37	0.1024	13	30695 (207)	30584 (210)	429 (3)	1.275 (115)	2.04 (22)	11.59
18222+1440.....	18 22 15.8	+14 40 13	0.1262	9	37821 ( )	37699 (34)	534 (1)	1.009 (91)	<1.93	11.47–11.71
18315+2249.....	18 31 30.6	+22 49 40	0.1310	2	39287 (131)	39151 (135)	556 (2)	0.868 (61)	<2.06	11.44–11.72
18585+2148.....	18 58 32.2	+21 48 58	0.1114	9	33396 ( )	33224 (31)	468 (0)	0.624 (87)	<1.93	11.14–11.49
19040+3356.....	19 04 04.1	+33 56 12	0.1812	5	54322 (300)	54151 (302)	787 (5)	0.715 (50)	1.11 (12)	11.86
19084+3719.....	19 08 29.7	+37 19 11	0.1091	2	32697 (179)	32525 (181)	457 (3)	0.742 (67)	2.81 (31)	11.59
19348+3400.....	19 34 50.4	+34 00 04	0.1030	9	30889 ( )	30684 (28)	430 (0)	0.638 (38)	<11.26	11.08–11.98
19458+0944.....	19 45 52.0	+09 44 31	0.1000	4	29964 (9)	29729 (30)	416 (0)	3.947 (395)	7.11 (64)	12.07
19559+1618.....	19 55 54.2	+16 18 06	0.1396	9	41853 ( )	41607 (27)	593 (0)	0.880 (70)	<2.26	11.50–11.80
20318+2343.....	20 31 52.5	+23 43 21	0.1011	9	30302 ( )	30025 (23)	420 (0)	0.944 (104)	<2.96	11.23–11.58
20322+1849.....	20 32 14.1	+18 49 45	0.1069	2	32038 (111)	31756 (113)	446 (2)	0.749 (67)	1.40 (31)	11.42
20344+0619.....	20 34 26.2	+06 19 45	0.1645	2	49306 (116)	49017 (118)	707 (2)	0.768 (115)	1.59 (24)	11.85
20361+1216.....	20 36 09.7	+12 16 51	0.1320	2	39575 (118)	39285 (120)	558 (2)	0.725 (65)	0.94 (9)	11.54
20394+2302.....	20 39 26.4	+23 02 12	0.1053	2	31568 (300)	31283 (301)	439 (4)	0.925 (65)	<1.92	11.26–11.52
20398+2745.....	20 39 53.4	+27 45 28	0.1025	9	30715 ( )	30437 (22)	426 (0)	1.434 (115)	<8.28	11.43–11.94
20402+1642.....	20 40 12.5	+16 42 27	0.1378	2	41313 (106)	41021 (108)	584 (2)	0.952 (86)	1.16 (9)	11.69
20450+0913.....	20 45 05.3	+09 13 19	0.1218	2	36520 (123)	36221 (125)	512 (2)	0.678 (54)	1.43 (17)	11.52
20460+1925.....	20 46 01.8	+19 25 49	0.1810	14	54262 (300)	53967 (301)	784 (5)	0.883 (62)	<1.45	11.74–11.96
21026+1042.....	21 02 39.9	+10 42 04	0.1078	2	32316 (115)	32002 (117)	449 (2)	0.578 (52)	<1.48	11.08–11.38
21064+2155.....	21 06 29.4	+21 55 35	0.1076	2	32257 (300)	31949 (301)	449 (4)	0.598 (48)	1.40 (13)	11.37
21135+0553.....	21 13 30.0	+05 52 55	0.1058	2	31732 (120)	31409 (121)	441 (2)	0.744 (67)	<2.04	11.17–11.48
21167+0819.....	21 16 42.7	+08 18 57	0.1015	2	30443 (138)	30117 (139)	422 (2)	0.568 (51)	1.31 (30)	11.29
21251+1114.....	21 25 11.7	+11 14 46	0.1140	2	34190 (317)	33859 (317)	477 (5)	0.598 (54)	0.79 (9)	11.32
21256+0219.....	21 25 40.3	+02 19 25	0.2570	16	77047 (300)	76716 (300)	1154 (5)	0.285 (43)	<0.65	11.59–11.86
21329+0705.....	21 32 56.0	+07 05 52	0.1165	5	34926 (300)	34589 (300)	488 (4)	0.696 (56)	0.85 (16)	11.40
21444+3534.....	21 44 25.3	+35 34 34	0.1518	9	45523 ( )	45220 (19)	648 (0)	0.913 (100)	<1.93	11.59–11.85
22057+0739.....	22 05 46.7	+07 39 25	0.1178	2	35315 (300)	34960 (300)	493 (4)	0.630 (151)	1.27 (23)	11.45
22068+2703.....	22 06 49.6	+27 02 59	0.1550	5	46467 ( )	46133 (14)	662 (0)	0.640 (83)	0.82 (22)	11.63
22416+1621.....	22 41 38.8	+16 21 11	0.1945	2	58321 (104)	57960 (104)	848 (2)	0.587 (59)	<1.66	11.63–11.95
22428+3215.....	22 42 50.7	+32 15 44	0.1572	2	47130 (114)	46799 (115)	673 (2)	0.652 (65)	<3.23	11.48–11.94
22541+0833.....	22 54 12.8	+08 33 27	0.1661	13	49799 (42)	49431 (42)	713 (1)	1.200 (192)	1.48 (27)	11.96

Note.—Units of right ascension are hours, minutes, and seconds, and units of declination are degrees, arcminutes, and arcseconds (B1950.0).

[a] FSC.

[b] km s^{-1}.

[c] h_{75}^{-1} Mpc.

[d] Jy.

[e] h_{75}^{-2} $L_{\odot}$.

References.—Redshifts were obtained from: (1) Kim & Sanders (1998); (2) W. Saunders (1999, personal communication); (3) Beers et al. (1995); (4) Downes, Solomon, & Radford (1993); (5) Leech et al. (1994); (6) Hill et al. (1988); (7) van Driel, van den Broek, & Baan (1995); (8) Strauss et al. (1992); (9) Nakanishi et al. (1997); (10) Strauss & Huchra (1988); (11) Kim et al. (1995); (12) Schmidt & Green (1983); (13) Fisher et al. (1995); (14) Vader et al. (1993); (15) de Grijp et al. (1992); (16) Schneider, Schmidt, & Gunn (1994); (17) Allen, Roche, & Norris (1985).

TABLE 2

OH NONDETECTIONS: OH LIMITS AND 1.4 GHz PROPERTIES

IRAS Name[a] (1)	$z_{\odot}$ (2)	$\log L_{\rm FIR}$ [b] (3)	$\log L_{\rm OH}^{\rm pred}$ [b] (4)	$\log L_{\rm OH}^{\rm max}$ [b] (5)	$t_{\rm on}$ [c] (6)	rms[d] (7)	$f_{1.4\ \rm GHz}$ [e] (8)	Class (9)	Note (10)
02290+3139.....	0.2115	11.99	2.53	2.11	20	0.46	3.6 (0.5)		4
03477+2611.....	0.1494	11.71	2.15	2.03	8	0.76	4.1 (0.5)		2
03533+2606.....	0.1883	11.46–12.05	1.79–2.61	1.85	40	0.32	6.7 (0.5)		1, 4
04046+1011.....	0.1845	11.50–12.16	1.85–2.76	2.05	16	0.52	<5.0		1
08559+1053.....	0.1480	11.89	2.39	1.69	20	0.35	<5.0	S2 (1)	
13542+1040.....	0.1234	11.47	1.81	1.67	12	0.48	65.1 (2.4)		
14202+2615.....	0.1590	12.04	2.60	1.96	8	0.57	10.2 (0.6)	H (2)	
14203+3005.....	0.1141	11.56	1.93	1.68	8	0.58	18.9 (1.0)	S1.9 (6)	
15445+3312.....	0.1558	11.52	1.88	2.12	4	0.85	<5.0	L (7)	1
15543+3013.....	0.1213	11.25	1.50	1.85	4	0.77	<5.0	H (7)	1, 2
15597+3133.....	0.1437	11.54	1.91	1.88	8	0.59	<5.0		
16045+2733.....	0.1139	11.56	1.93	1.61	12	0.50	9.7 (0.6)		
16121+2611.....	0.1310	10.79–11.05	0.86–1.23	1.94	4	0.80	18.2 (0.7)	S1.5 (8)	1, 6
16156+0146.....	0.1320	11.69	2.12	1.82	8	0.59	8.6 (0.5)	S2 (9)	
16284+2817.....	0.0970	11.39	1.70	1.46	16	0.44	4.2 (0.5)		
16474+3430.....	0.1115	11.88	2.38	1.66	8	0.59	11.5 (0.6)	H (2)	
17030+0457.....	0.1190	11.19–11.53	1.43–1.90	1.63	12	0.48	<5.0	S2 (1)	1
17156+1238.....	0.1134	11.26–11.47	1.51–1.81	1.81	4	0.80	4.8 (0.5)	H (3)	1, 3
17490+2659.....	0.1453	11.27–11.60	1.53–1.98	1.83	24	0.51	141.8 (4.3)	S1 (4)	1, 4
17574+0629.....	0.1096	11.65–11.96	2.06–2.48	1.48	16	0.40	14.6 (0.7)	H (2)	
18030+0705.....	0.1458	12.00	2.55	1.85	12	0.53	<5.0		
18040+2141.....	0.1016	11.64	2.05	1.42	24	0.41	5.7 (0.5)		
18147+1553.....	0.1024	11.59	1.97	1.45	16	0.43	53.4 (1.7)		
18222+1440.....	0.1262	11.47–11.71	1.81–2.14	1.75	8	0.57	<5.0		
18315+2249.....	0.1310	11.44–11.72	1.76–2.16	1.68	12	0.45	16.0 (0.7)		
18585+2148.....	0.1114	11.14–11.49	1.36–1.83	1.70	8	0.64	4.5 (0.7)		1
19040+3356.....	0.1812	11.86	2.35	2.00	20	0.48	3.1 (0.5)		
19084+3719.....	0.1091	11.59	1.98	1.57	16	0.50	<5.0		
19348+3400.....	0.1030	11.08–11.98	1.27–2.51	1.49	12	0.47	3.3 (0.6)		1
19458+0944.....	0.1000	12.07	2.64	1.53	8	0.55	15.3 (1.0)		2
19559+1618.....	0.1396	11.50–11.80	1.85–2.26	1.78	16	0.50	50.8 (2.2)		
20318+2343.....	0.1011	11.23–11.58	1.48–1.96	1.49	16	0.49	3.3 (0.5)		1
20322+1849.....	0.1069	11.42	1.74	1.76	12	0.81	3.3 (0.6)		1
20344+0619.....	0.1645	11.85	2.33	1.99	12	0.58	4.5 (0.5)		
20361+1216.....	0.1320	11.54	1.90	1.77	12	0.54	3.0 (0.6)		
20394+2302.....	0.1053	11.26–11.52	1.52–1.87	1.34	32	0.32	6.6 (0.5)		
20398+2745.....	0.1025	11.43–11.94	1.75–2.45	1.71	4	0.80	14.8 (0.7)		
20402+1642.....	0.1378	11.69	2.11	1.84	12	0.59	6.4 (1.5)		2
20450+0913.....	0.1218	11.52	1.88	1.84	12	0.76	9.8 (1.0)		
20460+1925.....	0.1810	11.74–11.96	2.19–2.48	2.12	12	0.64	18.9 (0.7)	S2 (5)	5
21026+1042.....	0.1078	11.08–11.38	1.27–1.68	1.40	32	0.35	10.4 (0.6)		1
21064+2155.....	0.1076	11.37	1.67	1.65	12	0.63	5.4 (0.5)		
21135+0553.....	0.1058	11.17–11.48	1.39–1.83	1.60	12	0.58	10.7 (1.1)		1
21167+0819.....	0.1015	11.29	1.56	1.41	24	0.40	7.8 (0.6)		
21251+1114.....	0.1140	11.32	1.60	1.50	32	0.39	<5.0		
21256+0219.....	0.2570	11.59–11.86	1.97–2.35	2.37	12	0.56	3.6 (0.6)		1
21329+0705.....	0.1165	11.40	1.71	1.59	20	0.46	2.4 (0.5)		
21444+3534.....	0.1518	11.59–11.85	1.98–2.34	1.89	20	0.54	14.8 (0.6)		
22057+0739.....	0.1178	11.45	1.77	1.66	12	0.54	3.1 (0.6)		
22068+2703.....	0.1550	11.63	2.03	1.97	12	0.63	4.3 (0.5)		2
22416+1621.....	0.1945	11.63–11.95	2.04–2.48	2.04	20	0.46	<5.0		
22428+3215.....	0.1572	11.48–11.94	1.82–2.46	1.99	12	0.63	8.8 (0.5)		1
22541+0833.....	0.1661	11.96	2.49	1.86	24	0.42	5.7 (0.6)	S2 (9)	

NOTES.—(1) Source needs more integration time, based on $L_{\rm OH}^{\rm pred} < L_{\rm OH}^{\rm max}$; (2) source needs more integration time, because of a suggestive feature in the bandpass; (3) galaxy pair—both nuclei have spectral type H II (Elston, Cornell, & Lebofsky 1985); (4) standing waves in the bandpass; (5) Sey 2/obscured Sey 1 (Frogel et al. 1989), BLR (Veilleux, Sanders, & Kim 1997); (6) Optically variable QSO (Maccacaro, Garilli, & Maereghetti 1987).

[a] FSC.

[b] $h_{75}^{-2}\ L_{\odot}$.

[c] Minutes.

[d] mJy.

[e] mJy. 1.4 GHz continuum fluxes are courtesy of the NRAO VLA Sky Survey (Condon et al. 1998).

REFERENCES.—Spectral classifications were obtained from: (1) Hill et al. (1988); (2) Kim et al. (1998); (3) Elston et al. (1985); (4) de Grijp et al. (1992); (5) Frogel et al. (1989); (6) Moran et al. (1996); (7) Veilleux et al. (1995); (8) Dahari & de Robertis (1988); (9) Veilleux, Kim, & Sanders (1999).

= low-ionization emission region (LINER). References for the classifications are listed in parentheses and included at the bottom of the table. Column (10): source notes, listed at the bottom of the table.

An estimate of the confidence of nondetections among the sample can be found from a comparison of $L_{\rm OH}^{\rm pred}$ to $L_{\rm OH}^{\rm max}$. Note, however, that the scatter in the $L_{\rm OH}$-$L_{\rm FIR}$ relation is quite large: roughly 0.5 orders of magnitude in $L_{\rm FIR}$ and 1 order of magnitude in $L_{\rm OH}$ (see Kandalian 1996). Among the nondetections, six out of 53 galaxies have $L_{\rm OH}^{\rm pred} < L_{\rm OH}^{\rm max}$, indicating that longer integration times are needed to confirm these nondetections. Eight out of 53 candidates have $L_{\rm OH}^{\rm max}$ within the range of $L_{\rm OH}^{\rm pred}$ set by an upper limit on f_{100} (we exclude from these tallies two sources with strong standing wave patterns because their rms does not reflect true noise levels). Integration times were a compromise between efficient use of telescope time and the requirement for a meaningful upper limit on the $L_{\rm OH}$ of nondetections. Given the scatter of identified OHMs about the $L_{\rm OH}$-$L_{\rm FIR}$ relation, we estimate that there are perhaps four additional OHMs among the nondetections, but this estimate relies on uncertain statistics of small numbers. A thorough analysis of the detection completeness will be performed once the survey is complete.

Strong continuum sources ($S_{1.4\ \rm GHz} \gtrsim 100$ mJy) produce standing waves between the Gregorian dome and the primary reflector, which frustrates detection of 1–10 mJy spectral lines. It may be possible to remove standing waves through a "double-switching" process by observing a pure continuum source of comparable flux density. For the present, the source that produced strong standing waves was set aside for later reobservation, and no upper limit on $L_{\rm OH}$ was calculated. The correlation between radio continuum and FIR flux density of megamaser hosts implies a correlation between radio continuum and OH megamaser emission due to the $L_{\rm OH}$-$L_{\rm FIR}$ relation (see Staveley-Smith et al. 1992), indicating that the removal of strong continuum sources from the sample might create a strong selection effect. Of the four observed OHM candidates exhibiting standing waves, however, only two have $S_{1.4\ \rm GHz} > 100$ mJy, as determined from the NRAO VLA Sky Survey (Condon et al. 1998). The other two are contaminated by continuum sources close to the target or falling in a side lobe of the main beam. These two were not excluded by their own properties, but by a random process. Hence, their exclusion should not bias the survey.

3.2. OH *Detections*

Tables 3 and 4 list, respectively, the optical/FIR and radio properties of the 12 new OH detections. Spectra of the 11 OHMs and the single OH absorber appear in Figure 1. The column headings of Table 3 are identical to those of Table 1. Table 4 lists the OH emission/absorption properties and 1.4 GHz flux density of the OH detections in the following format. Column (1): *IRAS* FSC name. Column (2): measured heliocentric velocity of the 1667.358 MHz line, defined by the center of the FWHM of the line. The uncertainty in the velocity of the line center is estimated assuming an uncertainty of ± 1 channel (± 49 kHz) on each side of the line. Column (3): on-source integration time in minutes. Column (4): peak flux density of the 1667.359 MHz OH line in mJy. Column (5): equivalent width–like measure in MHz. W_{1667} is the ratio of the integrated 1667.359 MHz line flux to its peak flux. Column (6): observed FWHM of the 1667.359 MHz OH line in MHz. Column (7): rest-frame FWHM of the 1667.359 MHz OH line in km s^{-1}. The rest-frame width was calculated from the observed width using the relation $\Delta v_{\rm rest} = c(1+z)(\Delta v_{\rm obs}/v_0)$. Column (8): hyperfine ratio, defined by $R_H = F_{1667}/F_{1665}$, where F_v is the integrated flux density across the emission/absorption line centered on v. $R_H = 1.8$ in thermodynamic equilibrium and increases as the degree of saturation of masing regions increases. In many cases, the 1665 MHz OH line is not apparent or is blended into the 1667 MHz OH line, and a good measure of R_H becomes difficult without a model for the line profile. It is also not

TABLE 3

OH Detections: Optical Redshifts and FIR Properties

IRAS Name[a] (1)	α (2)	δ (3)	$z_\odot$ (4)	Ref. z (5)	$v_\odot$ [b] (6)	$v_{\rm CMB}$ [b] (7)	D_L [c] (8)	$f_{60\,\mu\rm m}$ [d] (9)	$f_{100\,\mu\rm m}$ [d] (10)	$\log L_{\rm FIR}$ [e] (11)
06487+2208	06 48 45.1	+22 08 06	0.1437	2	43080 (300)	43206 (302)	618 (5)	2.070 (166)	2.36 (26)	12.07
16300+1558	16 30 05.6	+15 58 02	0.2417	1	72467 (64)	72515 (73)	1084 (1)	1.483 (134)	1.99 (32)	12.43
17539+2935	17 54 00.1	+29 35 50	0.1085	1	32525 (58)	32441 (67)	456 (1)	1.162 (58)	1.36 (19)	11.56
18368+3549	18 36 49.5	+35 49 36	0.1162	3	34825 (40)	34688 (51)	489 (1)	2.233 (134)	3.83 (27)	11.96
18588+3517	18 58 52.4	+35 17 04	0.1067	1	31973 (35)	31810 (46)	447 (1)	1.474 (103)	1.75 (33)	11.64
20248+1734	20 24 52.3	+17 34 24	0.1208	1	36219 (87)	35943 (90)	508 (1)	0.743 (82)	2.53 (38)	11.66
20286+1846	20 28 39.9	+18 46 37	0.1347	5	40396 (127)	40117 (129)	571 (2)	0.925 (74)	2.25 (16)	11.78
20450+2140	20 45 00.1	+21 40 03	0.1284	5	38480 (111)	38189 (113)	542 (2)	0.725 (51)	1.90 (15)	11.64
21077+3358	21 07 45.9	+33 58 05	0.1764	5	52874 (117)	52587 (119)	763 (2)	0.885 (88)	<1.55	11.72–11.95
21272+2514	21 27 15.1	+25 14 39	0.1508	5	45208 (120)	44890 (121)	643 (2)	1.075 (118)	<1.63	11.66–11.86
22116+0437	22 11 38.6	+04 37 29	0.1939	5	58144 (118)	57787 (118)	845 (2)	0.916 (73)	<1.03	11.82–11.98
19154+2704[f]	19 15 29.7	+27 04 32	0.0994	4	29792 ( )	29601 (30)	414 (0)	1.502 (120)	2.85 (23)	11.66

Note.—Units of right ascension are hours, minutes, and seconds, and units of declination are degrees, arcminutes, and arcseconds (B1950.0).

[a] FSC.

[b] km s^{-1}.

[c] h_{75}^{-1} Mpc.

[d] Jy.

[e] $h_{75}^{-2}\ L_\odot$.

[f] *IRAS* 19154+2704 is an OH absorber.

References.—Redshifts were obtained from: (1) Fisher et al. (1995); (2) Lu & Freudling (1995); (3) Strauss et al. (1992); (4) Nakanishi et al. (1997); (5) W. Saunders (1999, personal communication).

TABLE 4

OH Detections: OH Line and 1.4 GHz Continuum Properties

IRAS Name[a] (1)	$v_{1667,\odot}$[b] (2)	t_{on}[c] (3)	f_{1667}[d] (4)	W_{1667}[e] (5)	Δv_{1667}[f] (6)	Δv_{1667}[g] (7)	R_H (8)	log L_{FIR}[h] (9)	log L_{OH}^{pred}[h] (10)	log L_{OH}[h] (11)	$f_{1.4\,GHz}$[i] (12)
06487+2208	43017 (12)	28	7.60	0.85	1.03	211	6.1	12.07	2.63	2.86	10.8 (0.6)
16300+1558	72528 (12)	16	3.12	0.56	0.59	131	...	12.43	3.14	2.81	7.9 (0.5)
17539+2935	32522 (12)	80	0.76	0.72	0.81	161	≥ 2.9	11.56	1.93	1.74	4.0 (0.6)
18368+3549	34832 (12)	32	4.58	1.79	2.10	421	~ 9.5	11.96	2.48	2.83	21.0 (0.8)
18588+3517	31686 (12)	32	7.37	0.56	0.32	64	5.1	11.64	2.05	2.50	5.9 (0.5)
20248+1734	36538 (12)	48	2.61	1.36	0.88	177	~ 6.8	11.66	2.07	2.51	< 5.0
20286+1846	40471 (12)	24	15.58	1.51	1.10	224	≥ 4.4	11.78	2.23	3.38	< 5.0
20450+2140	38398 (12)	44	2.27	0.67	0.71	144	≥ 6.2	11.64	2.05	2.21	5.0 (0.5)
21077+3358	52987 (12)	28	5.04	1.86	1.15	243	≥ 7.4	11.72–11.95	2.16–2.47	3.23	9.4 (1.0)
21272+2514	45032 (12)	32	16.33	1.87	1.27	263	13.7	11.66–11.86	2.07–2.34	3.63	4.4 (0.5)
22116+0437	58180 (12)	68	1.76	1.16	0.56	121	~ 5.2	11.82–11.98	2.30–2.52	2.74	8.4 (0.6)
19154+2704[j]	29894 (12)	32	−2.62	0.85	0.93	184	1.81	11.66	2.07	...	63.6 (2.0)

[a] FSC.
[b] km s^{-1}.
[c] Minutes.
[d] mJy.
[e] MHz.
[f] MHz. Δv_{1667} is the *observed* FWHM.
[g] km s^{-1}. Δv_{1667} is the *rest-frame* FWHM. The rest-frame and observed widths are related by $\Delta v_{rest} = c(1 + z)(\Delta v_{obs}/v_0)$.
[h] $h_{75}^{-2}\ L_\odot$.
[i] mJy. 1.4 GHz continuum fluxes are courtesy of the NRAO VLA Sky Survey (Condon et al. 1998).
[j] *IRAS* 19154+2704 is an OH absorber.

clear that the two lines should have similar profiles, particularly if the lines are aggregates of many emission regions in different saturation states. Some spectra allow a lower limit to be placed on R_H, indicated by a greater than symbol. Blended or noisy lines have uncertain values of R_H and are indicated by a tilde. For *IRAS* 16300+1558, RFI makes any estimate of the hyperfine ratio impossible. Column (9): logarithm of the FIR luminosity, as in Table 3. Column (10): predicted OH luminosity log L_{OH}^{pred}, as in Table 2. Column (11): logarithm of the measured isotropic OH line luminosity, which includes the integrated flux density of both the 1667.359 and the 1665.4018 MHz lines. Note that L_{OH}^{pred} is generally less than the actual L_{OH} detected (nine out of 11 detections), as expected from Malmquist bias. Column (12): 1.4 GHz continuum fluxes from the NRAO VLA Sky Survey (Condon et al. 1998). If no continuum source lies within 30″ of the *IRAS* coordinates, an upper limit of 5.0 mJy is listed.

The spectra of the OH detections are shown in Figure 1. The abscissae and inset redshifts refer to the optical heliocentric velocity, and the arrows indicate the expected velocity of the 1667.359 (*left*) and 1665.4018 (*right*) MHz lines based on the optical redshift, with error bars indicating the uncertainty in the redshift. The spectra refer to 1667.359 MHz as the rest frequency for the velocity scale. *IRAS* 19154+2704 has no velocity uncertainty available in the literature.

In order to quantitatively identify somewhat dubious 1665 MHz OH line detections, we compute the autocorrelation function (ACF) of each spectrum and locate the secondary peak (the primary peak corresponds to zero offset, or perfect correlation). Any correspondence of features between the two main OH lines will enhance the second autocorrelation peak and allow us to identify 1665 MHz lines unambiguously, based not strictly on spectral location and peak flux, but on line shape as well. The secondary peak in the ACF of each spectrum, when present, is indicated by a small solid line. We expect the offset of the secondary peak to be equal to the separation of the two main OH lines, properly redshifted: (1.9572 MHz)/(1 + z). The *expected* location of the secondary ACF peak is indicated in Figure 1 by a small dashed line over each spectrum. Both the expected and actual secondary peak correlation positions are plotted offset with respect to the center of the 1667 MHz line, as defined by the center of the FWHM rather than the peak flux.

The expected relationship between the hyperfine ratio and the value of the secondary peak in the ACF should provide an upper limit on the actual size of the secondary peak. In the limit of perfect correspondence of features between the two main OH lines, the ACF second peak value becomes $R_H/(1 + R_H^2)$. Hence one might measure the correspondence between the 1667 and 1665 MHz lines by normalizing the actual secondary peak value to this upper limit. We will explore the utility of this line correspondence measure when we obtain a larger sample of OHMs.

We make some observations and measurements specific to individual OH detections as follows.

06487+2208. This merger was originally misclassified as Galactic cirrus by Strauss et al. (1992), but a redshift was measured in the QDOT survey (Lu & Freudling 1995). The OH spectrum shows both the 1667 and 1665 MHz lines and a strong correspondence of features between the two. The ACF has a strong secondary peak and is in excellent agreement with the predicted location of the 1665 MHz line, based on both the optical redshift and the frequency of the 1667 MHz line (the dotted and solid lines in Fig. 1 overlap). An *HST* WFPC2 archive image[4] shows a disturbed morphology and multiple nuclei (see Fig. 2). A Palomar 200 inch telescope spectrum indicates that the bright nuclei of

[4] Based on observations made with the NASA/ESA *Hubble Space Telescope*, obtained from the data archive at the Space Telescope Science Institute. STScI is operated by the Association of Universities for Research in Astronomy, Inc. under NASA contract NAS 5-26555.

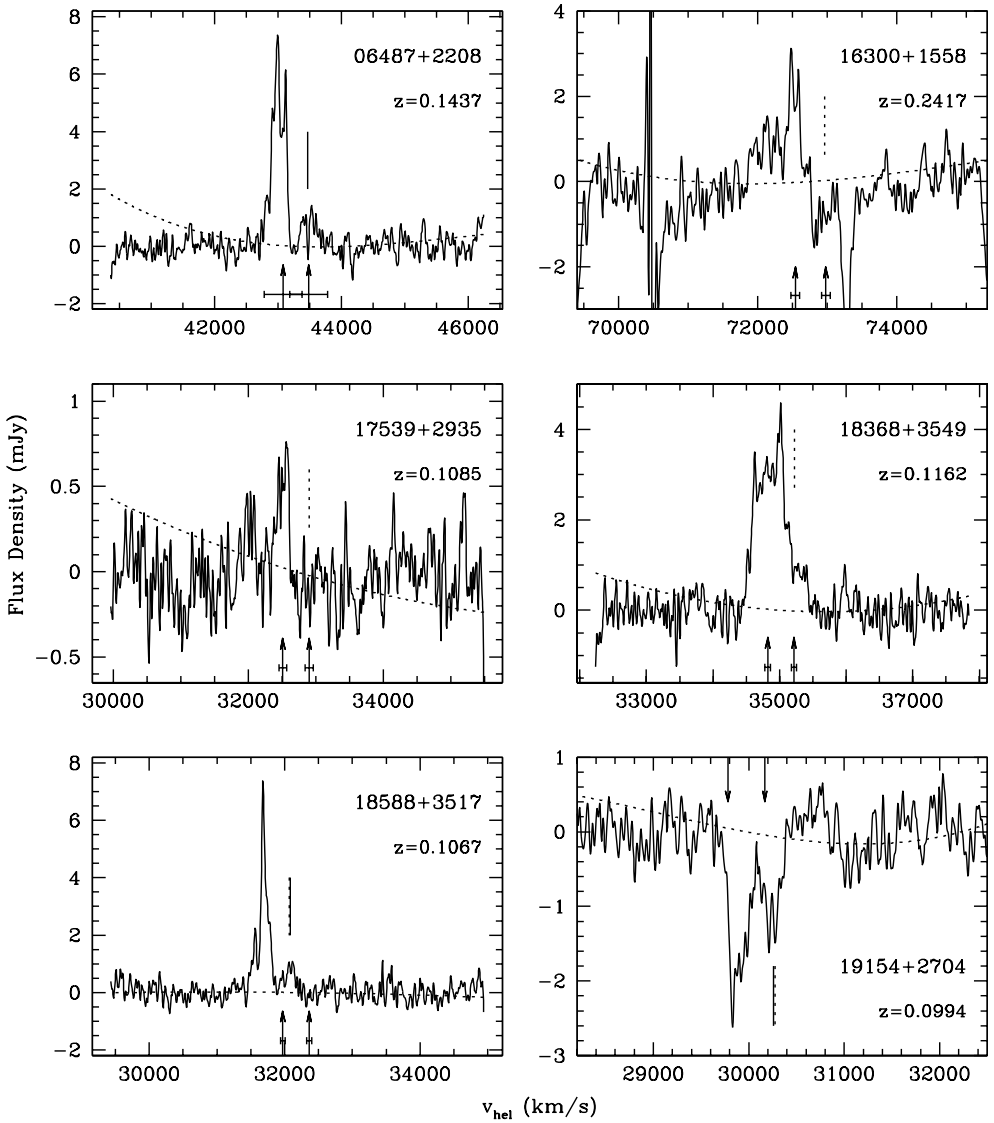

FIG. 1.—New OH megamasers/OH absorber discovered in ULIRGs. Abscissae and inset redshifts refer to the optical heliocentric velocity. Spectra use the 1667.359 MHz line as the rest frequency for the velocity scale. Arrows indicate the expected velocity of the 1667.359 (*left*) and 1665.4018 (*right*) MHz lines based on the optical redshift, with error bars indicating the uncertainty in the redshift. Solid vertical lines indicate the location of the secondary maximum in the autocorrelation function, and dashed vertical lines indicate the expected position of the 1665 MHz line, based on the centroid of the 1667 MHz line. The dotted baselines indicate the shape (but not the absolute magnitude) of the baselines subtracted from the calibrated spectra. The properties of these megamasers are listed in Tables 3 and 4.

this source show a composite of H II and LINER characteristics, based on the Osterbrock spectral line ratio classification method (Osterbrock 1989; Veilleux et al. 1995). The spectral line data and analysis will be presented in a later paper, when we have obtained optical spectra of a large number of OHMs. The nuclei of this source may have different properties and result in a net blend of emission region types in a spectrum that is spatially unresolved from the ground.

16300+1558. This is the second most distant OHM known, at $z_{\odot} = 0.2417$ (*IRAS* 14070+0525 has $z_{\odot} = 0.2644$—see Baan et al. 1992). Optically, Kim, Veilleux, & Sanders (1998) classify it as a LINER. The observed bandpass is disturbed by several RFI features, including a feature that obliterates the 1665 MHz line region. Hence no hyperfine ratio can be measured for this source, and no autocorrelation analysis can be performed. The 1667 MHz line velocity agrees with the optical redshift to within the uncertainty of 64 km s^{-1}. Note that the shape of the 1667 MHz line is strikingly similar to that of *IRAS* 06487+2208. Both have a double-peaked structure, which suggests either multiple maser sites or a rotating masing torus, as in III Zw 35 (Diamond et al. 1999). *IRAS* 16300+1558 is the most FIR-luminous source observed in our candidate list to date, but its OH luminosity falls short of the L_{OH} predicted from L_{FIR}. Reobservation in quieter RFI conditions would be desirable in order to detect the 1665 MHz line and confirm the OH luminosity of this exceptional object.

17539+2935. The primary OH line detected in this object corresponds with the optical redshift prediction for the 1667 MHz line. No corresponding 1665 MHz line is visible in the spectrum. A secondary OH line of marginal signal-to-noise is blueshifted with respect to the primary line by 462 km s^{-1} in the rest frame. The second OH line

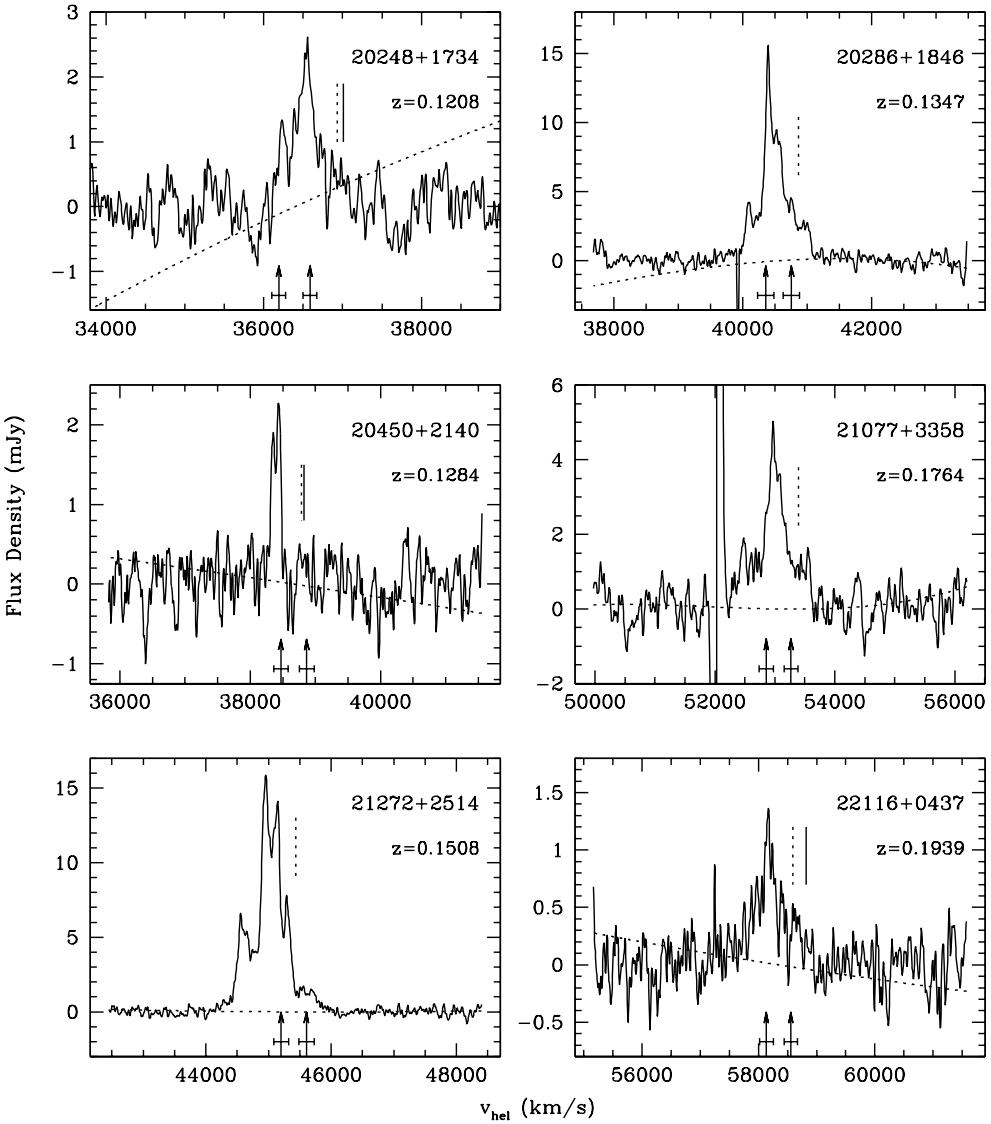

FIG. 1.—*Continued*

suggests a double-nucleus host, with each nucleus producing OH emission. The Digitized Sky Survey[5] image reveals an extended spidery morphology, which could be attributed to expelled merger debris. More integration time on this source is needed to detect the 1665 MHz line and to confirm the blueshifted component. The hyperfine ratio can only be given an upper limit for this source. We assume a square profile of width equal to the 1667 MHz line width and height 1 σ to obtain $R_H \geq 2.9$.

18368+3549. This source shows a broad OH line profile ($\Delta v_{1667} = 421$ km s^{-1}), which includes several sharp components. The hyperfine ratio listed in Table 4 assumes that the small shoulder on the high-velocity side of the main line is the 1665 MHz line. There is likely some blending of lines, which would tend to decrease R_H. The Digitized Sky Survey image shows an extended source with irregular morphology, but IR and optical imaging by Murphy et al. (1996) shows this object to have a single nucleus, or if double, a nuclear separation of $<0\farcs8$ (<1.5 kpc) in K band (the upper limit is set by the seeing). The r-band image shows a slightly disturbed morphology, while the K-band image is nearly unresolved. As expected of any OHM host, *IRAS* 18368+3549 is rich in molecular gas which is concentrated in a small nuclear volume. Solomon et al. (1997) measure a CO(1–0) line width of 330 km s^{-1}, estimate a H_2 mass of $3.9 \times 10^{10}\ M_\odot$ and derive a blackbody radius of 299 pc.

18588+3517. This OHM has no broad emission component evident and appears to be dominated by a pair of sharp features at 1667 MHz. The 1667 and 1665 MHz lines show a remarkable correspondence, which indicates a much larger hyperfine ratio for the main peak than for the smaller, lower velocity peak. Hence, the main peak is the more saturated of the two. The optical redshift is significantly larger (~ 300 km s^{-1}) than the observed line velocity. This could be due to an underestimated error in the optical redshift or

[5] Based on photographic data obtained using Oschin Schmidt Telescope on Palomar Mountain. The Palomar Observatory Sky Survey was funded by the National Geographic Society. The Oschin Schmidt Telescope is operated by the California Institute of Technology and Palomar Observatory. The plates were processed into the present compressed digital format with their permission. The Digitized Sky Survey was produced at the Space Telescope Science Institute (STScI) under grant NAG W-2166.

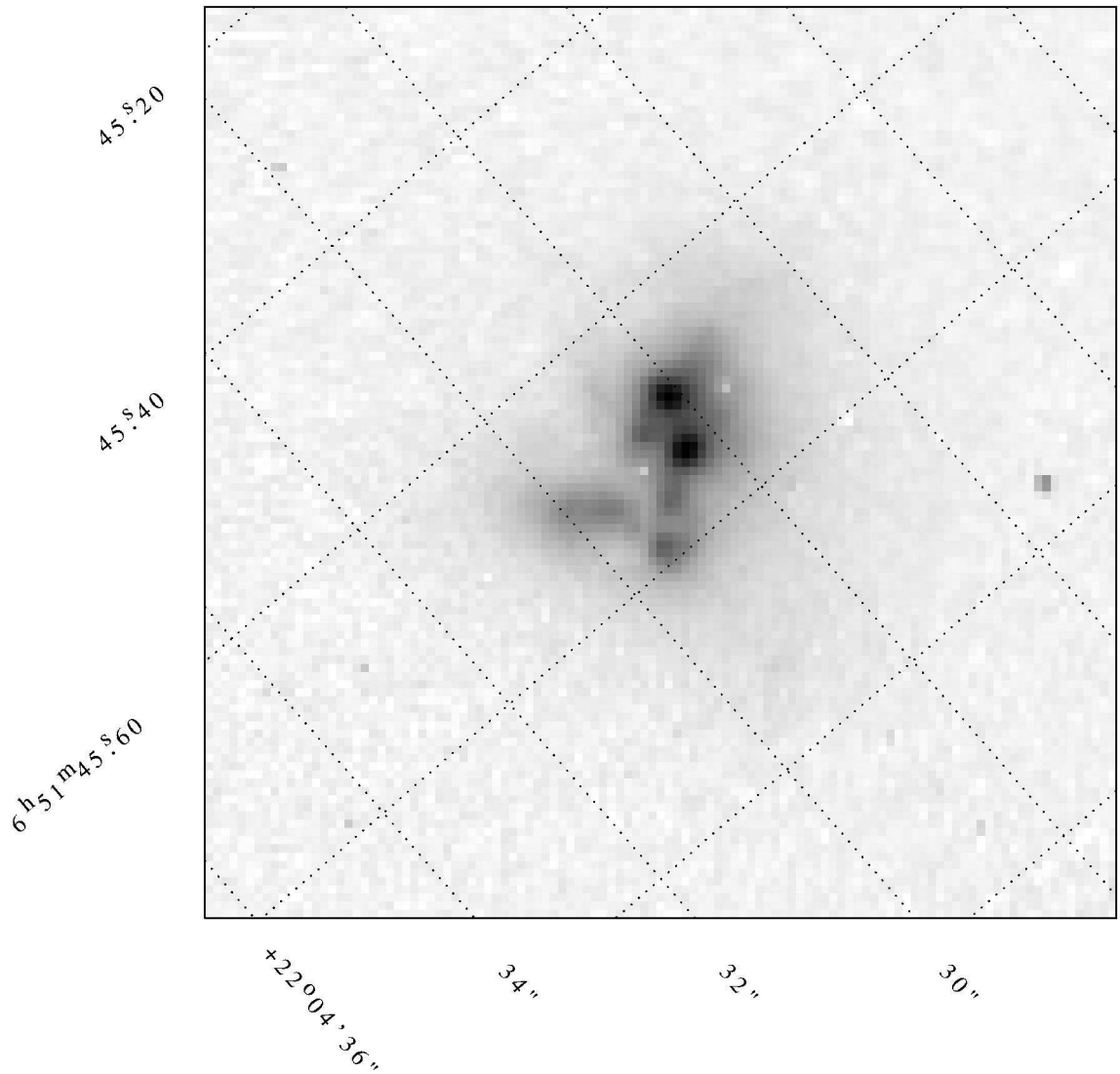

FIG. 2.—*HST* WFPC2 archive image[4] of *IRAS* 06487+2208 ($z_{\odot} = 0.1437$) taken with the F814W filter ($\lambda = 7940$ Å, $\Delta\lambda = 1531$ Å). The image reveals a disturbed morphology and multiple nuclei. Total integration time was 800 s, taken in two exposures of 400 s for cosmic-ray removal. Coordinate labels are in epoch J2000.0. The disturbed morphology is not evident in ground-based observations with ~1".5 seeing.

to a double nucleus source: the OH emission may come from an obscured nucleus, while the optically brighter nucleus may be responsible for the observed optical redshift. This explanation seems plausible because OH maser emission favors high gas column densities, but optical line observations omit high-extinction environments.

19154+2704. This is an OH absorber, with $R_H = 1.81$, which is consistent with the hyperfine ratio in thermodynamic equilibrium ($R_H = 1.8$). There is good agreement between the optical redshift and the observed velocity of the absorption lines (note that the optical redshift has no uncertainty available in the literature). The 1665 MHz absorption line is strong and has a velocity in good agreement with the ACF secondary peak and line separation predictions. The host has a fairly strong 1.4 GHz continuum (64 mJy), which creates some mild standing waves in the baseline.

20248+1734. The OH spectrum of this source shows significant continuum emission within the 3'.2 beam (~75 mJy at 1.487 GHz). The closest NVSS source to *IRAS* 20248+1734 is 1'.9 distant and has a 1.4 GHz flux of 209 mJy (Condon et al. 1998). Contamination from the NVSS source may be responsible for the mild standing waves evident in the OH spectrum. These standing waves contaminate the emission lines and may be creating an artificial 1665 MHz line, as well as broadening the 1667 MHz line. A higher signal-to-noise spectrum is required to remove the contamination. The ACF and 1667 MHz line centroid both identify a spectral feature as the 1665 MHz line, but this feature is not significantly different from other baseline standing waves. The optical redshift differs significantly from the observed OH line velocity.

20286+1846. This OHM shows both broad and sharp spectral components. The very broad "shoulders" of the OH emission (rest-frame $\Delta v = 1040$ km s^{-1} at 10% peak flux) suggest a spatially extended region of diffuse emission. The total OH luminosity emitted by this object is unusually strong, $\log(L_{\rm OH}/L_{\odot}) = 3.33$, more than an order of magnitude larger than predicted from $L_{\rm FIR}$: $\log(L_{\rm OH}^{\rm pred}/L_{\odot}) = 2.15$. Identification of the 1665 MHz line is difficult because of the blending of the lines. Moving from high velocity to low, the first and second peaks have the correct separation from the third and fourth peaks, respectively, to be 1665 MHz

lines. The optical redshift and 1667 MHz line centroid both agree with this identification. Assuming this to be true, we measure a hyperfine ratio of $R_H = 4.4$. On the other hand, the low-velocity shoulder indicates that it is possible to have broad 1667 MHz emission far from the peak, so all of the high-velocity emission could be strictly 1667 MHz. Hence, we say $R_H \geq 4.4$. Since OH masing is beamed emission, which relies on a pump and stimulant, it is possible that only blueshifted foreground emission should appear along the line of sight. If, however, there is a torus of emission, high- and low-velocity features might be expected to be symmetrical about the center line. There is currently not enough information to break the degeneracy in the physical emission configurations of this OHM.

20450+2140. No broad component is evident in the OH spectrum of this source, nor is any 1665 MHz emission detected. The ACF and expected line separation both indicate a marginal feature to be the 1665 MHz line. This feature is identical to several other noise features in the baseline, so we can only compute a lower limit on the hyperfine ratio, $R_H \geq 6.2$. The spectrum suggests two sharp emission components but could in fact be a single line modified by detector noise.

21077+3358. The OH spectrum shows both broad and sharp components, including broad shoulders similar to *IRAS* 20286+1846 (rest-frame $\Delta v = 1330$ km s^{-1} at 10% peak flux). The high-velocity shoulder may either be broad 1667 MHz emission or the 1665 MHz line. If we assume the latter, then $R_H = 7.4$. If there is any 1667 mixing into this component, which seems probable given the appearance of the low-velocity shoulder, then R_H will be larger. Hence, we conclude that $R_H \geq 7.4$. The ACF makes no prediction for the location of the 1665 MHz line (it shows no secondary peak), but the expected line separation indicates a 1665 MHz line centroid position in the center of the high-velocity shoulder. Poor subtraction of Galactic H II produced the feature at 52,000 km s^{-1}.

21272+2514. This OHM is the third most luminous known [$\log (L_{\rm OH}^{\rm pred}/L_\odot) = 3.63$] at a redshift of $z = 0.1508$. Its observed $L_{\rm OH}$ is more than an order of magnitude greater than we predict from $L_{\rm FIR}$. The spectrum exhibits multiple peaks and a rest-frame width of 849 km s^{-1} at 10% of peak flux. The 1665 MHz line can be identified based on the optical redshift. The measurement of $R_H = 13.7$ given in Table 4 assumes that there are no 1665 MHz lines associated with the 1667 MHz peaks with velocities below the optical redshift. As indicated in Figure 1, the centroid of the 1667 MHz emission falls below the optical redshift, and the ACF shows no secondary maximum.

22116+0437. The Digitized Sky Survey image of the host galaxy shows a possible galaxy pair in a single envelope. The two spectral lines show good correspondence with the optical redshift predictions. Despite the low luminosity of this OHM, $L_{\rm OH}$ is greater than $L_{\rm OH}^{\rm pred}$ by a factor of ~ 2. This is the third most distant OHM detected to date, at $z = 0.1939$.

4. DISCUSSION

Detection of 11 new OHMs out of the 65 candidates observed yields a success rate of one in six (17%). Figure 3 plots $L_{\rm FIR}$ versus FIR color ($f_{100\,\mu{\rm m}}/f_{60\,\mu{\rm m}}$) for all 65 candidates, plus one previously known OHM included in the survey sample that was observed for a system check at the telescope. As indicated by the histograms in the right-hand panels, there is a strong tendency for OHMs to appear in the most FIR-luminous LIRGs. Any explicit lower bound on $L_{\rm FIR}$ would increase the detection rate (we have no such $L_{\rm FIR}$ selection criterion), but we hesitate to impose a constraint that depends on choice of cosmology. Also, we have low confidence in the nondetections in the lowest $L_{\rm FIR}$ bin because they generally have $L_{\rm OH}^{\rm max} > L_{\rm OH}^{\rm pred}$. There may yet be OHMs lurking among these nondetections. A FIR color-selection criterion would also boost the detection rate, but it would cause the loss of some detections. *Any* color-selection criterion would exclude the 63 *IRAS* galaxies in the survey sample, which are undetected at 100 μm. Many of these have strong 60 μm fluxes and are thus interesting survey targets.

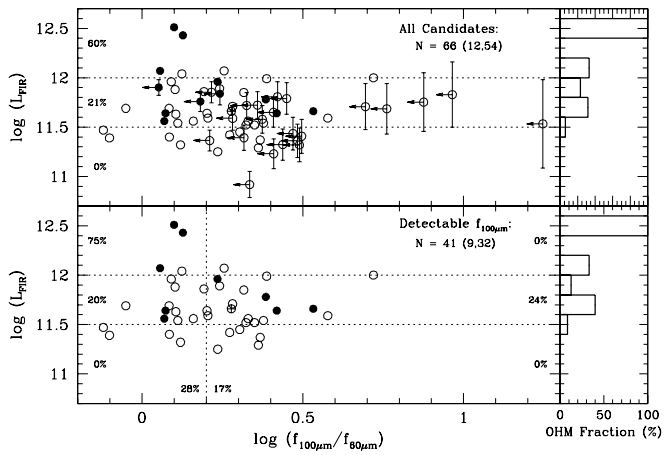

FIG. 3.—Observed OH megamaser candidates. The two left panels show $L_{\rm FIR}$ vs. FIR color for candidates observed to date, and the two right panels show the OHM fraction as a function of $L_{\rm FIR}$. Filled circles mark OHMs, open circles mark nondetections, and the crossed circle marks the OH absorber. Points with error bars are nondetections at 100 μm. Vertical error bars indicate the possible range of $L_{\rm FIR}$, constrained by $f_{60\,\mu{\rm m}}$ and an upper limit on $f_{100\,\mu{\rm m}}$. Horizontal arrows indicate upper limits on FIR color. Inset percentages indicate the OHM fraction for each sector delineated by the dashed lines. The upper panels plot all 65 candidates observed, plus one known OHM reobserved to check the observing setup in 1999 April. The bottom panels plot the 41 objects with detected $f_{100\,\mu{\rm m}}$. The inset numbers follow the key: N = observed (OHMs, nondetections). We use $H_0 = 75$ km s^{-1} Mpc^{-1}.

The new OHMs show a wide range of properties. They span two decades in OH luminosity and range from very narrow (64 km s^{-1}) single lines to broad (421 km s^{-1}), complicated multiline ensembles to sharp lines atop broad bases of emission. The sample shows diverse hyperfine ratios, with hints that the ratio may vary within a single source, indicating a range of maser saturation states. None of the new OHMs are strong radio continuum sources (the strongest is 21 mJy), and there does not appear to be a correlation between OH flux and radio continuum flux. There appears to be a positive relationship between the OH luminosity of the new OHMs and the 1667 MHz line widths, opposite the trend found by Staveley-Smith et al. (1992) and Kandalian (1996). This relationship will be explored further with a larger sample. Only two of the new OHMs have optical spectral classifications (Kim et al. 1998 classify *IRAS* 16300+1558 as a LINER, and we classify *IRAS* 06487+2208 as a LINER/H II mixture), but the nondetections cover the full range of spectral types, from H II regions to LINERs to all Seyfert classifications. Baan et al. (1998) classified the bulk of the known sample of OHMs

and found a tendency for OHMs to occur in active nuclei. Optical classification of the new higher redshift sample is under investigation and will be reported when the study is complete.

5. CONCLUSIONS

We have demonstrated the ability of the upgraded Arecibo telescope to detect new OH megamasers with a high success rate (one in six) in the highest OHM redshift regime in short integration times. The detection rate is due in part to the improved frequency agility and sensitivity of the upgraded Arecibo telescope, and it is in part due to completion of *IRAS* galaxy redshift surveys (most notably the PSCz).

The survey will produce a set of about 50 new OHMs in short order, which will double the sample and greatly enhance the population at the highest redshifts. The new sample will be used to explore the physics of OHM phenomena in a statistically meaningful manner and to evaluate theoretical models of OHM environments and excitation mechanisms.

The OHM detection rate of our flux-limited survey sample will produce an accurate measure of the incidence of OHMs in ULIRGs as a function of host properties, which is much less subject to the small number statistics than previous surveys. Subsequent searches for OHMs will be able to indirectly measure the FIR luminosity function of ULIRGs at various redshifts, which can be related to the merger rate of galaxies as a function of cosmic time.

The authors are very grateful to Will Saunders for access to the PSCz catalog, to Liese van Zee and Martha Haynes for providing the optical spectrum of *IRAS* 06487+2208, and to the staff of NAIC for observing assistance and support. This research was supported by Space Science Institute archival grant 8373 and made use of the NASA/IPAC Extragalactic Database (NED), which is operated by the Jet Propulsion Laboratory, California Institute of Technology, under contract with the National Aeronautics and Space Administration. We acknowledge the use of NASA's SkyView facility[6] located at NASA Goddard Space Flight Center.

[6] At http://skyview.gsfc.nasa.gov.

REFERENCES

Abraham, R. G. 1999, IAU Symp. 186, Galaxy Interactions at Low and High Redshift, ed. D. B. Sanders & J. Barnes (Dordrecht: Kluwer), 11
Allen, D. A., Roche, P. F., & Norris, R. P. 1985, MNRAS, 213, 67P
Baan, W. A. 1989, ApJ, 338, 804
———. 1991, in ASP Conf. Ser. 16, Atoms, Ions, and Molecules: New Results in Spectral Line Astrophysics (San Francisco: ASP), 45
Baan, W. A., Haschick, A., & Henkel, C. 1992, AJ, 103, 728
Baan, W. A., Rhoads, J., Fisher, K., Altschuler, D. R., & Haschick, A. 1992, ApJ, 396, L99
Baan, W. A., Salzer, J. J., & LeWinter, R. D. 1998, ApJ, 509, 633
Beers, T. C., Kriessler, J. R., Bird, C. M., & Huchra, J. P. 1995, AJ, 109, 874
Briggs, F. H. 1998, A&A, 336, 815
Brinchmann, J., et al. 1998, ApJ, 499, 112
Burdyuzha, V. V. & Komberg, B. V. 1990, A&A, 234, 40
Clements, D. L., Saunders, W. J., & McMahon, R. G. 1999, MNRAS, 302, 391
Clements, D. L., Sutherland, W. J., McMahon, R. G., & Saunders, W. 1996, MNRAS, 279, 477
Condon, J. J., Cotton, W. D., Greisen, E. W., Yin, Q. F., Perley, R. A., Taylor, G. B., & Broderick, J. J. 1998, AJ, 115, 1693
Cowie, L. L., & Barger, A. J. 2000, in The Hy-Redshift Universe: Galaxy Formation and Evolution at High Redshift, ed. A. J. Bunker & W. van Breugel (San Francisco: ASP), in press
Dahari, O. & de Robertis, M. M. 1988, ApJS, 67, 249
de Grijp, M. H. K., Keel, W. C., Miley, G. K., Goudfrooij, P., & Lub, J. 1992, A&AS, 96, 389
Diamond, P. J., Lonsdale, C. J., Lonsdale, C. J., & Smith, H. E. 1999, ApJ, 511, 178
Downes, D., Solomon, P. M., & Radford, S. J. E. 1993, ApJ, 414, L13
Ellis, R. S., Colless, M., Broadhurst, T., Heyl, J., & Glazebrook, K. 1996, MNRAS, 280, 235
Elston, R., Cornell, M. E., & Lebofsky, M. J. 1985, ApJ, 296, 106
Fisher, K. B., Huchra, J. P., Strauss, M. A., Davis, M., Yahil, A., & Schlegel, D. 1995, ApJS, 100, 69
Frogel, J. A., Gillett, F. C., Terndrup, D. M., & Vader, J. P. 1989, ApJ, 343, 672
Fullmer, L. & Lonsdale, C. J. 1989, Cataloged Galaxies and Quasars Observed in the IRAS Survey (Pasadena: JPL)
Henkel, C., Güsten, R., & Baan, W. A. 1987, A&A, 185, 14
Hill, G. J., Heasley, J. N., Becklin, E. E., & Wynn-Williams, C. G. 1988, AJ, 95, 1031
Kandalian, R. A. 1996, Astrophysics, 39, 237
Kim, D.-C. & Sanders, D. B. 1998, ApJS, 119, 41
Kim, D.-C., Sanders, D. B., Veilleux, S., Mazzarella, J. M., & Soifer, B. T. 1995, ApJS, 98, 129
Kim, D.-C., Veilleux, S., & Sanders, D. B. 1998, ApJ, 508, 627
Leech, K. J., Rowan-Robinson, M., Lawrence, A., & Hughes, J. D. 1994, MNRAS, 267, 253
Le Févre, O., et al. 2000, MNRAS, 311, 565
Lilly, S. J., Tresse, L., Hammer, F., Crampton, D., Le Févre, O. 1995, ApJ, 455, 108
Lineweaver, C. H., Tenorio, L., Smoot, G. F., Keegstra, P., Banday, A. J., & Lubin, P. 1996, ApJ, 470, 38
Lu, N. Y., & Freudling, W. 1995, ApJ, 449, 527
Maccacaro, T., Garilli, B., & Mereghetti, S. 1987, AJ, 93, 1484
Moran, E. C., Helfand, D. J., Becker, R. H., & White, R. L. 1996, ApJ, 461, 127
Murphy, T. W., Jr., Armus, L., Matthews, K., Soifer, B. T., Mazzarella, J. M., Shupe, D. L., Strauss, M. A., & Neugebauer, G. 1996, AJ, 111, 1025
Nakanishi, K., Takata, T., Yamada, T., Takeuchi, T. T., Shiroya, R., Miyazawa, M., Watanabe, S., & Saito, M. 1997, ApJS, 112, 245
Norris, R. P., Gardner, F. F., Whiteoak, J. B., Allen, D. A., & Roche, P. F. 1989, MNRAS, 237, 673
Osterbrock, D. E. 1989, Astrophysics of Gaseous Nebulae and Active Galactic Nuclei (Mill Valley, CA: Univ. Sci.)
Patton, D. R., Pritchet, C. J., Yee, H. K. C., Ellingson, E., & Carlberg, R. G. 1997, ApJ, 475, 29
Sanders, D. B., Surace, J. A., & Ishida, C. M. 1999, in IAU Symp. 186, Galaxy Interactions at Low and High Redshift, ed. D. B. Sanders & J. Barnes (Dordrecht: Kluwer), 289
Saunders, W., et al. 2000, preprint (astro-ph/9909191)
Schmidt, M., & Green, R. F. 1983, ApJ, 269, 352
Schneider, D. P., Schmidt, M., & Gunn, J. E. 1994, AJ, 107, 1245
Smail, I., Ivison, R. J., Owen, F. N., Blain, A. W., & Kneib, J.-P. 2000, ApJ, 528, 612
Solomon, P. M., Downes, D., Radford, S. J. E., & Barrett, J. W. 1997, ApJ, 478, 144
Staveley-Smith, L., Norris, R. P., Chapman, J. M., Allen, D. A., Whiteoak, J. B., & Roy, A. L. 1992, MNRAS, 258, 725
Strauss, M. A., & Huchra, J. 1988, AJ, 95, 1602
Strauss, M. A., Huchra, J. P., Davis, M., Yahil, A., Fisher, K. B., & Tonry, J. 1992, ApJS, 83, 29
Vader, J. P., Frogel, J. A., Terndrup, D. M., & Heisler, C. A. 1993, AJ, 106, 1743
van Driel, W. V., van den Broek, & Baan, W. 1995, ApJ, 444, 80
Veilleux, S., Kim, D.-C., & Sanders, D. B. 1999, ApJ, 522, 113
Veilleux, S., Kim, D.-C., Sanders, D. B., Mazzarella, J. M., & Soifer, B. T. 1995, ApJS, 98, 171
Veilleux, S., Sanders, D. B., & Kim, D.-C. 1997, ApJ, 484, 92